Materials & Design 240 (2024) 112835

Contents lists available at ScienceDirect

Materials & Design

journal homepage: www.elsevier.com/locate/matdes

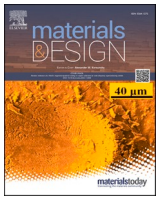

Self-assembled titanium-based macrostructures with hierarchical (macro-, micro-, and nano) porosities: A fundamental study

Matthew D. Wadge [a,*], Pearl A. Agyakwa [b], Reda M. Felfel [a,c,d], Richard Homer [a], Timothy P. Cooper [a,e], Zakhar R. Kudrynskyi [a], Edward Lester [a], Ifty Ahmed [a], David M. Grant [a,*]

[a] Advanced Materials Research Group, Faculty of Engineering, University of Nottingham, United Kingdom
[b] Power Electronics and Machines Centre Research Group, Faculty of Engineering, University of Nottingham, United Kingdom
[c] Physics Department, Faculty of Science, Mansoura University, Mansoura, Egypt
[d] Advanced Composites Group, University of Strathclyde, Glasgow, Scotland, United Kingdom
[e] Advanced Manufacturing Technology Research Group, Faculty of Engineering, University of Nottingham, United Kingdom

ARTICLE INFO

Keywords:
Self-assembly
Alkaline conversion
Sodium titanate
Nanoporous
Porous scaffold

ABSTRACT

This study details the novel self-assembly of sodium titanate converted Ti-based microspheres into hierarchical porous 3D constructs, with macro-, micro-, and nanoporosity, for the first time. Ti6Al4V microspheres were suspended into 5 M NaOH (60 °C/24 h) solutions, with extensive variations in microsphere:solution ratios to modify microsphere interaction and initiate self-assembly through proximity merging of titanate surface dendritic growth. The formed structures, which either produced 1) unbonded, sodium titanate-converted microspheres; 2) flat (non-macroporous) scaffolds; or 3) open, hierarchically porous scaffolds, were then assessed in terms of their formation mechanism, chemical composition, porosity, as well as the effect of post-heat treatments on compressive mechanical properties. It was found that specific microsphere:solution ratios tended to form certain structures (<$^1/_3$ powder, 0.5 to 3 porous, >3 flat non-macroporous, >8 powder) due to a combination of microsphere freedom of movement, H_2 gas bubble formation, and exposed surface reactivity. This promising discovery highlights the potential for lower temperature, simplistic production of 3D constructs with modifiable chemical properties due to the ion-exchange potential of titanate structures, with clear applications in a wide-range of fields, from medical materials to catalysts.

1. Introduction

The formation of nanoporous alkaline titanate structures *via* wet chemical conversion have been of interest in orthopaedic applications, specifically hip replacements and spinal fusion cages, for the past two decades [1–5], and have been extensively investigated due their ability to generate apatite *in vivo via* multi-step ion-exchange reactions [6–11]. These structures benefit from a simplistic production methodology (5 M NaOH, 60 °C, 24 h) [5], high level of porosity at the sub-micron scale [12], and enhanced tailorability due to their structure providing cationic exchange [13,14]. Significant strides have been made in the biomedical and energy fields regarding titanate structures, with emphasis on their cationic exchange [15–18], formation of nanotubes for drug delivery and other biomedical applications [19–23], as well as enhanced cellular proliferation on nanowhisker scaffolds [24].

Previous investigations have demonstrated the applicability of alkaline titanate nanostructures, with nanoporous morphologies, through translation onto alternative medical materials by applying a Ti layer (since their wet-chemical formation was previously limited to specific Ti-containing materials) [14]. The approach allows ion-exchange reactions to generate specific properties such as cytocompatibility and antibacterial effects [13], or to inhibit corrosion of Mg materials for biodegradable orthopaedic applications [14]. We have recently reported wet-chemically grown nanoporous titanate structures onto microspherical Ti6Al4V substrates [25] and their electrocatalytic potential [26]. The aforementioned studies introduced a novel property of these structures, which previously had not been investigated within the literature, and was an uncommon byproduct of the original papers. By utilising the cross-growth of alkaline titanate nanostructures as the bonding between converted Ti6Al4V microspheres, one can generate 3D structures with macro-, micro-, and nanoporosity that are generated purely through self-assembly. The utilisation of such structures has

* Corresponding authors.
E-mail addresses: matthew.wadge3@nottingham.ac.uk (M.D. Wadge), david.grant@nottingham.ac.uk (D.M. Grant).

https://doi.org/10.1016/j.matdes.2024.112835
Received 21 October 2023; Received in revised form 12 February 2024; Accepted 8 March 2024
Available online 11 March 2024

potential for a wide range of applications due to their ability to facilitate ion exchange reactions (useful for removal of harmful cations in solutions for water treatment applications), the variation in porosity (ideal for pore-entrapment of particles, bacteria, or viruses, as well as bone ingrowth for biomedical applications and increased surface area providing weight saving and improved efficiency for battery/energy technologies). This paper highlights insights into the formation mechanism of such structures, from the growth of the titanate coatings on Ti6Al4V microspheres, to the influence of vial size and microsphere: solution ratios on self-assembly and macrostructure conditions. Here we present work on exploring this exciting and novel potential platform technology to produce hierarchical self-assembling titanate macrostructures, with tailored porosity that have the capability of delivering unique structures for multiple applications across disciplines.

2. Materials and Methods

2.1. Powders

Plasma atomised Ti6Al4V Grade 23 powder (LPW Technologies, UK; Fig. 1), was utilised as the base material for the self-assembly study. The powder had D_{10}, D_{50}, and D_{90} values, calculated *via* a Mastersizer 3000 (Malvern, UK) laser diffraction method, of 19.6, 31.5 and 49.1 μm, respectively [27]. The unconverted microspheres are labelled Ti6Al4V_MS.

2.2. Wet-chemical conversion

The atomised powders were suspended in a *ca.* 5 M NaOH solution prepared using NaOH pellets (*ca.* 19.99 g per 100 mL of distilled water; 99.9 % purity; Sigma-Aldrich). Variations in the sphere-solution ratio used to explore the self-assembly mechanism are detailed in Table 1. Two different vial sizes were also used to gain some additional insight regarding available volume and the produced scaffolds, with narrow and wide referring to Falcon™ 15 mL (17 mm diam.; 120 mm length) and Nunc™ 50 mL (30 mm diam.; 90 mm length) Conical Sterile Polypropylene Graduated Centrifuge Tubes, respectively.

The varying ratios were nominally chosen in order to generate qualitatively identifiable viscosities, namely low sphere-solution ratios resulted in more of a suspension of spheres in excessive aqueous solutions, medium sphere-solution ratios resulted in an easily flowing suspension mixture with higher viscosity, and finally high sphere-solution ratios resulting in viscous mixtures or inadequate solution to powder mixtures. To produce such mixtures, nominal aliquots of the NaOH solution were dispensed into polypropylene containers, which contained previously fixed quantities of microspheres. These were then sealed, inverted, and heated in a furnace at 60±2 °C for 24 h. Unless vial type is stated, converted powders prior to heat-treatment have been labelled Ti6Al4V_MS_TC.

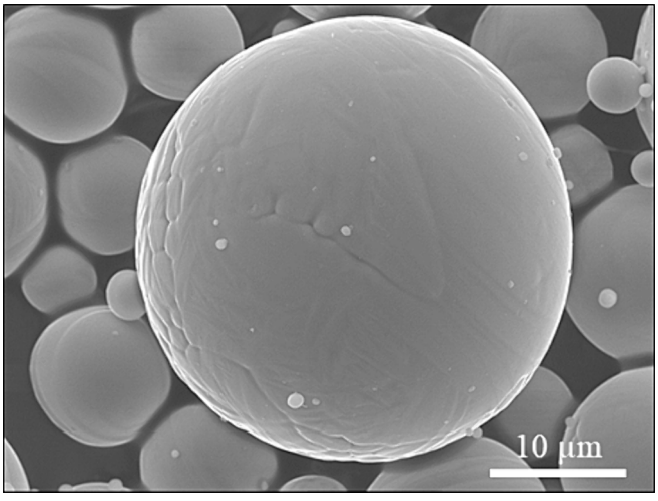

Fig. 1. Representative micrograph of Ti6Al4V_MS microspheres used in this study.

Table 1
Various nominal microsphere (g) to liquid (mL) ratios of Ti6Al4V microspheres in 5 M NaOH solution ordered from lowest to highest ratio (represented as both the simplified ratio and its decimal representation i.e., 1:10 = 0.1). Condition column details the end point condition of the samples, being either loose powder, flat/compact discs, or porous scaffolds. *Indicates fracturing of the produced sample (highlighting a mix of powder and porous). Two vial sizes were utilised in this study: wide (50 mL/30 mm diam.) and/or narrow (15 mL/17 mm diam.), which are highlighted in the Vial column.

Microspheres/g	Solution/mL	Ratio/g:mL (g/mL)	Final Condition	Vial
1	10	1:10 (0.1)	Powder	Both
1	5	1:5 (0.2)	Powder	Both
3	10	3:10 (0.3)	Powder	Both
2	5	2:5 (0.4)	Powder	Both
5	10	1:2 (0.5)	Porous	Narrow
5	10	1:2 (0.5)	Porous*	Wide
3	5	3:5 (0.6)	Porous	Narrow
5	5	1:1 (1)	Porous*	Narrow
5	5	1:1 (1)	Porous	Wide
8	8	1:1 (1)	Porous*	Narrow
8	8	1:1 (1)	Porous	Wide
10	10	1:1 (1)	Porous	Wide
3	2	3:2 (1.5)	Porous	Both
3.5	2	7:4 (1.75)	Porous	Wide
4	2	2:1 (2)	Porous	Wide
10	5	2:1 (2)	Porous	Both
3.4	1	17:5 (3.4)	Flat	Wide
3.5	1	7:2 (3.5)	Porous	Wide
3.9	1	39:10 (3.9)	Flat	Wide
10	2	5:1 (5)	Porous/Flat	Wide
7	1	7:1 (7)	Porous	Wide
10	1	10:1 (10)	Flat	Wide
10	1	10:1 (10)	Powder	Narrow
10	0.5	20:1 (20)	Flat	Wide
10	0.5	20:1 (20)	Powder	Narrow

Upon removal, the samples (whether formed scaffolds or microspheres) were washed *via* filtration in deionised water to remove excess NaOH, before furnace drying at 100 °C for 1 h (in air), followed by storage in a desiccator until testing.

2.3. Post Heat-Treatment

Representative samples were then heat-treated using a Lenton® furnace in air with a ramp rate of 5 °C.min^{-1} to 100 °C then left to dwell for 1 h. Then the furnace temperature was raised to 600 °C at the same ramp rate and dwell time, followed by furnace cooling to room temperature. For all analyses, these samples are labelled Ti6Al4V_MS_HT.

2.4. Characterisation

2.4.1. Scanning Electron Microscopy (SEM) & Energy Dispersive X-ray Spectroscopy (EDS)

Image acquisitions for higher resolution micrographs were conducted on a Field-Emission Gun Scanning Electron Microscope (JEOL 7100 FEG-SEM). Surface compositional analysis was determined *via* an Energy-Dispersive X-ray spectrometer (EDS) (Oxford Instruments) at a working distance of 10 mm, a beam voltage of 15 kV, whilst maintaining a minimum X-ray count of 150,000 counts.

2.4.2. X-ray Photoelectron Spectroscopy (XPS)

All samples were mounted onto stainless steel stubs using carbon sticky tabs. X-ray Photoelectron Spectroscopy (XPS) was conducted using a VG ESCALab Mark II X-ray photoelectron spectrometer with a

monochromatic Al Kα X-ray source incident to the sample surface at *ca.* 30°. Survey and high-resolution scans were conducted in addition to the measurement of adventitious C 1s for calibration: charge corrected to 284.8 eV. Parameters for acquisition were as follows: step size of 1 and 0.2 eV for survey and high-resolution scans, respectively; number of scans set at 5; dwell time 0.2 s for survey scans, and 0.4 s for high-resolution scans. Binding energies were measured over a range of 0–1200 eV. All spectra were analysed in Casa XPS constraining the Full Width at Half Maximum (FWHM) to the same value for all deconvoluted spectral peaks for the same element.

2.4.3. MicroCT

MicroCT was utilised to assess the level of internal porosity of representative scaffolds generated, specifically to assess the difference between flat compact scaffolds and what have been termed open porous scaffolds. Additionally, the effect on porosity level due to the post heat treatment was also assessed. For the scans, scaffolds were imaged using a Zeiss Xradia Versa XRM-500 platform. The X-ray source for the Xradia 500 Versa instrument was set to 140 kV and power of 10 W. The apparatus's macro lens (0.4X) was used with 360 degrees rotations. Multiple projection images acquired at different rotational angles, with projection images mathematically reconstructed to obtain a 3D model (filtered back projection algorithm). The average pixel size for empty pellets was 19.53 μm, with image acquisition parameters being the same for all samples. Both samples were scanned with 1600 projections per 360 degrees scan. Each 3D image stack contained 1016 slices with dimensions of 1024×1024 pixels and 24-bit depth.

Image segmentation was employed to assess the degree of porosity of the samples. Due to the variations in sample dimensions, cuboidal volumes of size 351×176×108 voxels (equivalent 6855×3437×2109 μm) (see supplementary information for schematic representation) were assessed, with 3 volumes per sample type. Porosity values were extracted through a binarise and open pore labelling, with 3D volumes calculated. Average pore sizes were taken per cuboidal volume with a total average of each sample type calculated from the 3 volumes. A flowchart of this process is included in the Supplementary Information.

2.4.4. X-ray diffraction (XRD)

All powders/scaffolds analysed were mounted into Perspex (polymethyl methacrylate; PMMA; Bruker) holders, ensuring the sample surface sits flush with the edge of the holder. Sample crystallinity was assessed using a Bruker D8 Advanced XRD spectrometer (Cu Kα source, λ = 1.5406 Å, 40 kV, 35 mA). Measurements were taken over a 2θ range from 20 to 60°; with a step size of 0.015° (2θ); a glancing angle of 1.2°; and a dwell time of 12–16 s. The glancing angle allows the X-ray beam to graze the surface, penetrating the first few microns of material, and restricting the diffraction signal to the same depth [28].

2.5. Mechanical testing

The compressive properties of the produced scaffolds were determined using a mechanical tester (Instron 5969 equipped with a 5 kN load cell) at a compression rate of 0.5 mm.min^{-1}, until complete compaction of the scaffold was seen. The setup of the test and calculations of compressive strength and modulus were performed in an appropriately modified test method, referencing both ASTM E9 (Standard Test Methods of Compression Testing of Metallic Materials at Room Temperature) and ISO 13314–2011 (Mechanical Testing of Metals – Ductility Testing – Compression Test for Porous and Cellular Metals). The standards above can be adapted for cellular lattice structures fabricated by additive manufacturing [29], and hence this was applied in this case as the produced scaffolds in the study are structurally comparable, since no set standard is available for the structures developed in this study. Compressive modulus was calculated as the gradient of the initial linear portion in the stress–strain curves. Although standardised sample sizes were not possible, most samples were found to be within set ranges. 3 samples were used for each condition. For the flat, narrow porous, and wide porous scaffolds, the height and width of the scaffolds have been detailed in Table 2.

Table 2
Height and width of all scaffolds tested via compression mechanical testing. Values given are mean values of all preparation conditions: Ti6Al4V_MS_TC (NaOH treated, no heat treatment); Ti6Al4V_MS_HT (600 °C heat treatment). Error values are standard error (n = 3).

Scaffold Type	Height (mm)	Width (mm)
Flat	7.4±1.3	21.6±0.4
Porous (Narrow)	10.9±1.1	13.3±0.1
Porous (Wide)	10.9±1.3	21.8±0.2

3. Results

3.1. Scaffold structure formation

Initially, an understanding of the optimal metallic microsphere to aqueous solution ratio was investigated to generate stable, reproducible scaffolds *via* titanate self-assembly. Multiple ratios were investigated resulting in a spectrum of viscosities, from a thick slurry (high sphere to solution ratio) to more of an aqueous suspension (low sphere to solution ratio). Additionally, the effect of different vessel sizes (narrow *vs.* wide) on the produced scaffolds was also investigated.

As can be seen in Fig. 2, the scaffolds have a structure, that fall into 3 broad classes: powder (Fig. 2A), porous (Fig. 2B and C), and flat (Fig. 2D). The powders are free flowing, similar to the pre-converted powder, with a noticeably darker appearance. Flat samples appear with no noticeable macroscopic porosity.

By combining all the results of the sphere:solution ratios, four regions were identified, as detailed in Fig. 3. Above a ratio of *ca.* 8, powder or flat scaffolds are more likely to be formed. Between *ca.* 3 and 8, porous or flat scaffolds are more likely to form. The optimal region occurs between *ca.* $^{1}/_{3}$ and 3, whereby porous scaffolds are more probable

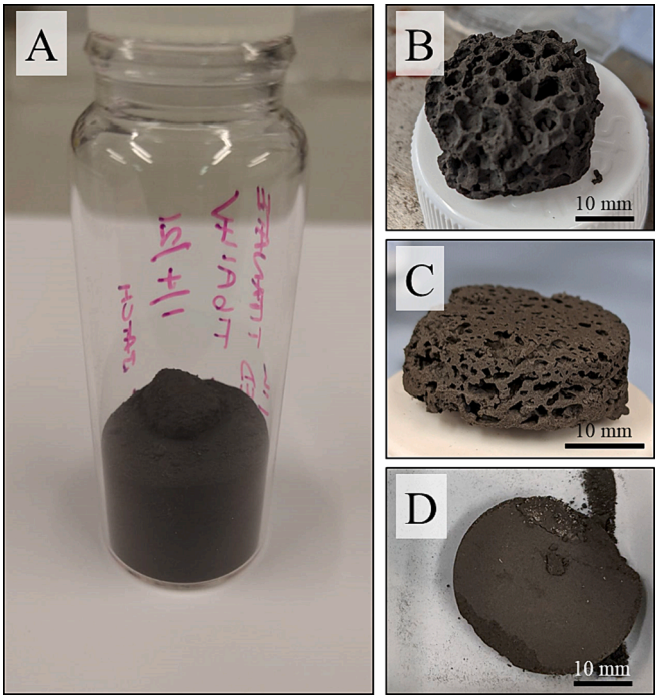

Fig. 2. Different possible morphologies of the produced samples. A) Converted powder (not self-assembled); B) Porous scaffold; C) Flat/Porous transition scaffold; D) Flat scaffold/sample.

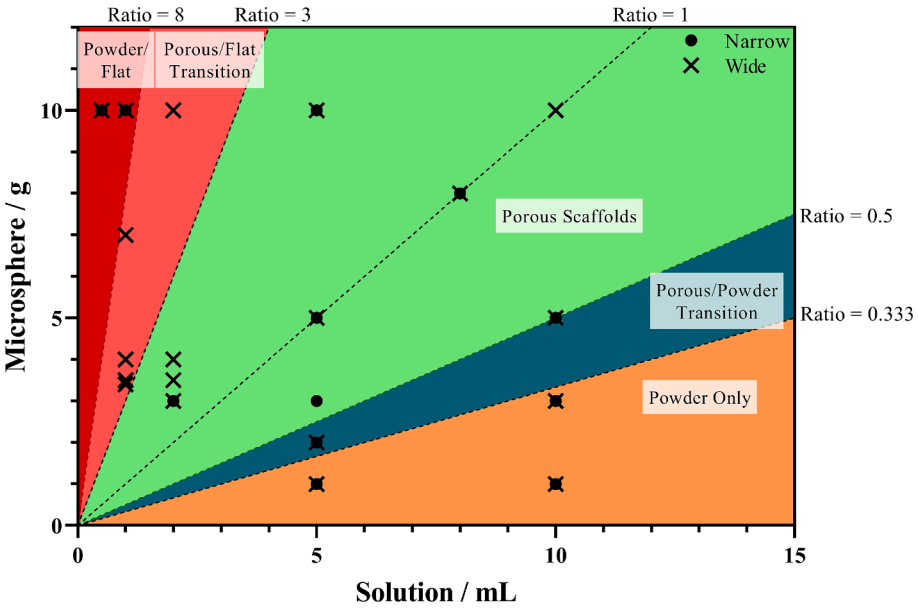

Fig. 3. Distribution of all tested sphere:solution ratios, with linear lines describing specific ratios, namely $^1/_3$, ½, 1, 3, and 8. Shaded regions were inserted to highlight predictable scaffold formations, or transition regions whereby two different states were observed to occur. Note, the regions highlighted are only a guide, and do not discount the possibility of alternative types of scaffold formation. Above a ratio of *ca.* 8, powder or flat scaffolds are more likely to be formed. Between *ca.* 3 and 8, porous or flat scaffolds are more likely to form. The 'goldilocks' region occurs between *ca.* $^1/_3$ and 3, whereby porous scaffolds are more probable to occur. A ratio of $<^1/_3$ mostly results in converted powder, with a powder/porous transition occurring between 0.5 and $^1/_3$.

to occur. A ratio of $<^1/_3$ results in converted powder, with a porous/powder transition region occurring between 0.5 and $^1/_3$. It was seen that the wider vessel provided a more consistent scaffold, as the narrow samples formed were too narrow and resulted in premature cracking of the structure. Ratios of 0.3, 1, 1.5, 10 and 20 were tested with both narrow and wide vessels (Table 1). Consistency between the vessels was seen for 0.3, 1 (although cracking was noted for the narrow samples), and 1.5 which produced powder, porous and porous samples, respectively. For the higher ratios of 10 and 20, the narrow samples produced powder for both, whereas the wide vessels generated flat scaffolds.

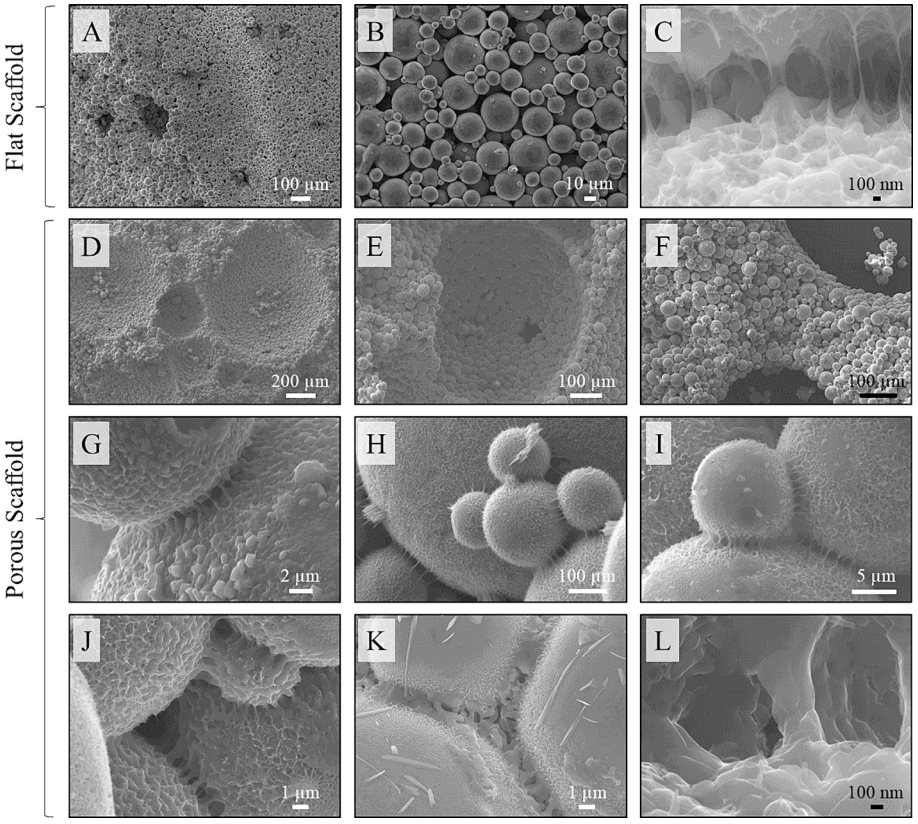

Fig. 4. SEM Micrographs of flat (A-C), and porous (D-L) scaffolds. (D-F) details the macroporosity, (G-I) details the individual spheres, including connections between; and (J-L) demonstrates the nanoporosity on the spheres, as well as a more detailed view of the interconnectedness.

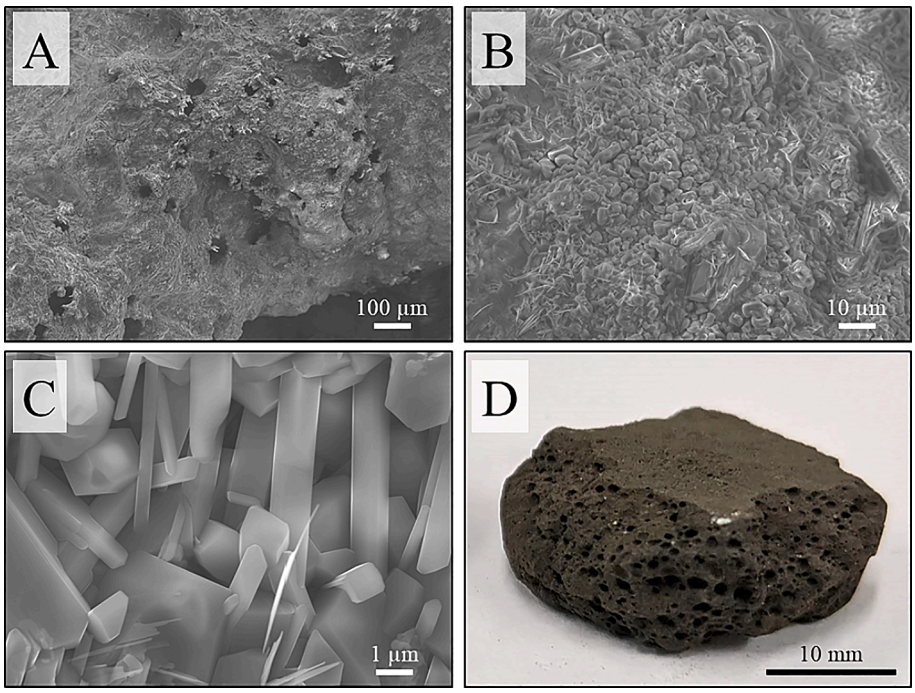

Fig. 5. SEM micrographs (A, B, and C) of varying magnifications showing the microstructure of a heat treated, NaOH converted porous scaffold (D).

3.2. SEM analysis

For the flat scaffolds (Fig. 4A – C), the majority of the surface is composed of interconnected microspheres, with minimal pore formation (*ca.* 100–200 μm diameter: (Fig. 4A) relative to the porous scaffolds. As can be seen for the lower magnification porous scaffold micrographs (Fig. 4D – F), larger (>200 μm) and high frequency of pores were noted. The porous structure is made of arranged, interconnected microspheres. The bonding between the samples (Fig. 4G – L) demonstrates overlapping of the nanoporous homogeneous structures on the surface of the converted microspheres.

Following heat-treatment of the porous NaOH structures, there is a distinct change in the microstructure of the produced scaffold (Fig. 5A – C), with a clear loss in visibility of the underlying microspheres. Additionally, at higher magnifications, the nanoporosity on the surface of the microspheres is no longer present, having been replaced with cuboidal (*ca.* 1 μm wide, >3 μm long) crystals (Fig. 5C). There is a subtle change at the macroscopic level, with a reduction in the size of the pores, and densification of the scaffold (Fig. 5D).

An understanding of the thickness of the produced nanoporous titanate structure on the surface of the microspheres was also ascertained. As can be seen in the representative SEM micrograph (Fig. 6), some microspheres demonstrated regions that had not converted, and therefore, were useful to calculate the thickness of the titanate structure. It was confirmed that the approximate thickness of the titanate structure on the microspheres was *ca.* 735±41 nm (Fig. 6).

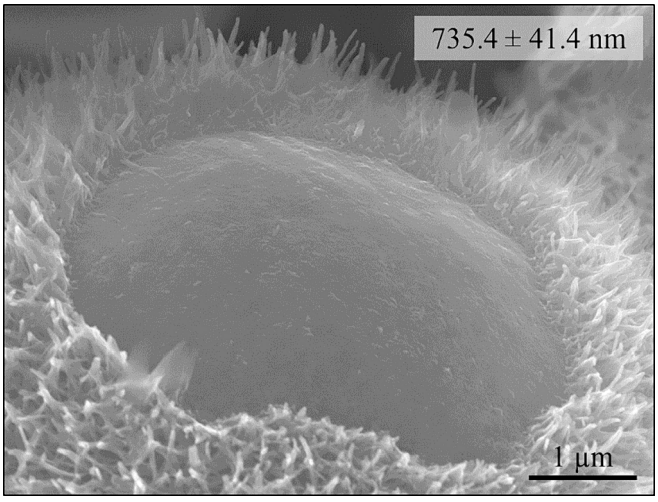

Fig. 6. Representative SEM micrograph of an exposed region of the titanate coating, enabling quantification of the thickness of the produced titanate structures. Thickness calculated via SEM, with the value given as mean with standard error (n = 5).

3.3. MicroCT

For the MicroCT analysis, representative samples were taken from the following collective groups: Porous (wide or narrow), Porous Heat Treated (wide or narrow), Flat (wide and non-porous), and Flat Heat Treated (wide and non-porous).

As can be seen from both the sub-volumes (Fig. 7) and the average calculated porosity (area, volume and equivalent diameter: Table 3) of each sample from the 3 sub-volumes, there are two key effects seen. A: the Porous labelled samples exhibited larger pores (pore volume: 6.01 (±2.50) × 10^8 μm^3) compared to the denoted 'Flat' samples (0.72 (±0.03) × 10^8 μm^3; *ca.* 10 times lower). B: heat treatment of the scaffolds is accompanied with a drop in average pore volume (6.01 (±2.50) × 10^8 to 2.17 (±0.46) × 10^8 μm^3 for the Porous and Porous Heat Treated, respectively; 0.72 (±0.03) × 10^8 to 0.23 (±0.05) × 10^8 μm^3 for the Flat and Flat Heat Treated, respectively), with the Flat Heat Treated sample having smaller pores compared to the Porous Heat Treated counterpart.

For the remainder of the experimental data, aside from the compression mechanical testing, samples were collated into three sample types, which were the control powder (Ti6Al4V_MS), the porous NaOH-converted scaffold (Ti6Al4V_MS_TC), and the heat treated NaOH-converted counterpart (Ti6Al4V_MS_HT). The justification for this being that these groups are chemically similar i.e., comparing unconverted powder, to titanate converted samples, to then heat-treated versions of the titanate converted samples.

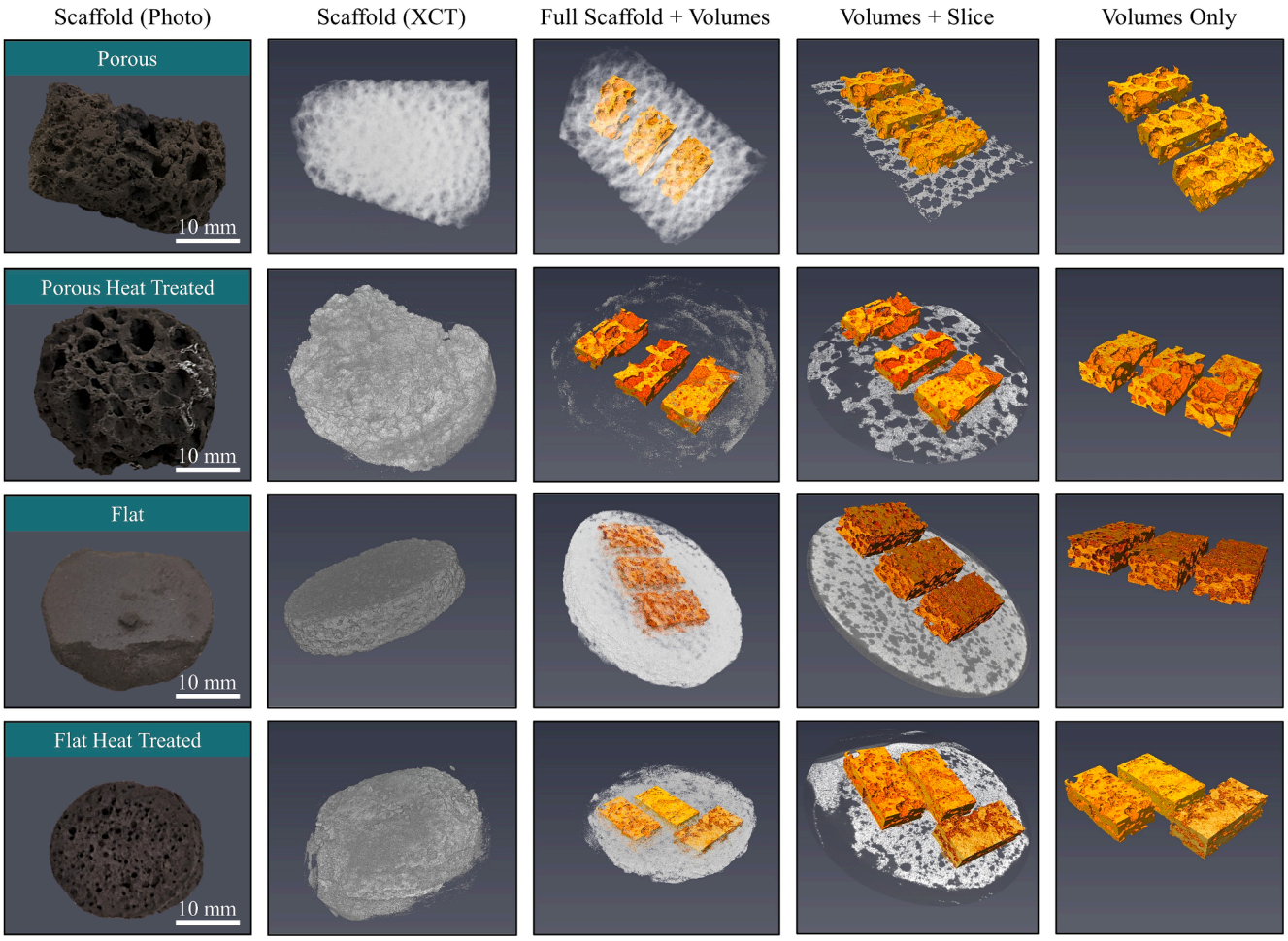

Fig. 7. XCT images and generated sub-volumes for pore size calculation. Slices and full scaffold included for sub-volume context.

3.4. EDS

Elemental analysis through the means of EDS was conducted (Fig. 8 & Table 4). For the porous scaffold prior to heat treatment, there was a clear concentration of Ti on the microspheres, with Ti also being present at the fusing points of the microspheres. The nanoporous coating, and the interconnected struts, were formed of Ti, Na and O, with clear concentration of O and Na at these points. Following heat-treatment, there was a reduction in Na content, with just Ti and O present in the cuboidal crystals formed.

It was clear from the quantitative EDS analysis (Table 4), that the presence of Na increased from *ca.* 0 to 15.1 at.% following NaOH conversion of the microspheres, as well as an increase in O content from *ca.* 0 to 59.8 at.%, and a decrease in Ti, V, and Al from *ca.* 86.2 to 23.4, 4.1 to 1.1, and 9.7 to 0.6 at.%, respectively. Subsequently, heat treatment of the sample also resulted in variations in the elemental composition of the samples. Na content reduced completely to just trace amounts, with a marked increase in Ti to *ca.* 65.4 at.%, and a decrease in O content to *ca.* 31.4 at.%. Al and V remained constant within the tolerance stated.

3.5. XRD

Crystallographic information was determined via XRD (Fig. 9). There was no discernible difference between the pre- and post-NaOH converted samples (Ti6Al4V_MS and Ti6Al4V_MS_TC, respectively), which both detailed peaks corresponding to HCP Ti (ICDD 00–044-1294). The lack of titanate peaks is likely due to sub-micron thickness and/or nanocrystallinity. Following heat treatment, as expected, conversion to TiO_2 was observed being with major phase being rutile (TiO_2: ICDD 00–021-1276). with minor phase of anatase (TiO_2: ICDD PDF 00–21-1272).

3.6. XPS

XPS quantification (Fig. 10, Table 5, & Table 6) demonstrated noticeable differences in the high-resolution O 1s (Fig. 10B), Ti 2p (Fig. 10C) and Na 1s (Fig. 10D) deconvolutions, peak intensity/presence, and elemental quantities between samples. In addition, differences were also noted in the survey spectra (Fig. 10A). Following NaOH treatment (Ti6Al4V_MS_TC) of the Ti6Al4V_MS powder, significant Na

Table 3
Average pore values (Pore Area, Equivalent Diameter, and Pore Volume) for the representative samples (porous and flat) and their respective heat treated counterparts.

Sample	Pore Area (μm^2)	Equivalent Diameter (μm)	Pore Volume (μm^3)
Porous	3.75 ($\pm$1.45) $\times$ 10^6	660.6$\pm$206.9	6.01 ($\pm$2.50) $\times$ 10^8
Porous Heat Treated	1.51 ($\pm$0.30) $\times$ 10^6	240.9$\pm$36.7	2.17 ($\pm$0.46) $\times$ 10^8
Flat	0.94 ($\pm$0.06) $\times$ 10^6	323.4$\pm$38.9	0.72 ($\pm$0.03) $\times$ 10^8
Flat Heat Treated	0.41 ($\pm$0.09) $\times$ 10^6	214.1$\pm$30.8	0.23 ($\pm$0.05) $\times$ 10^8

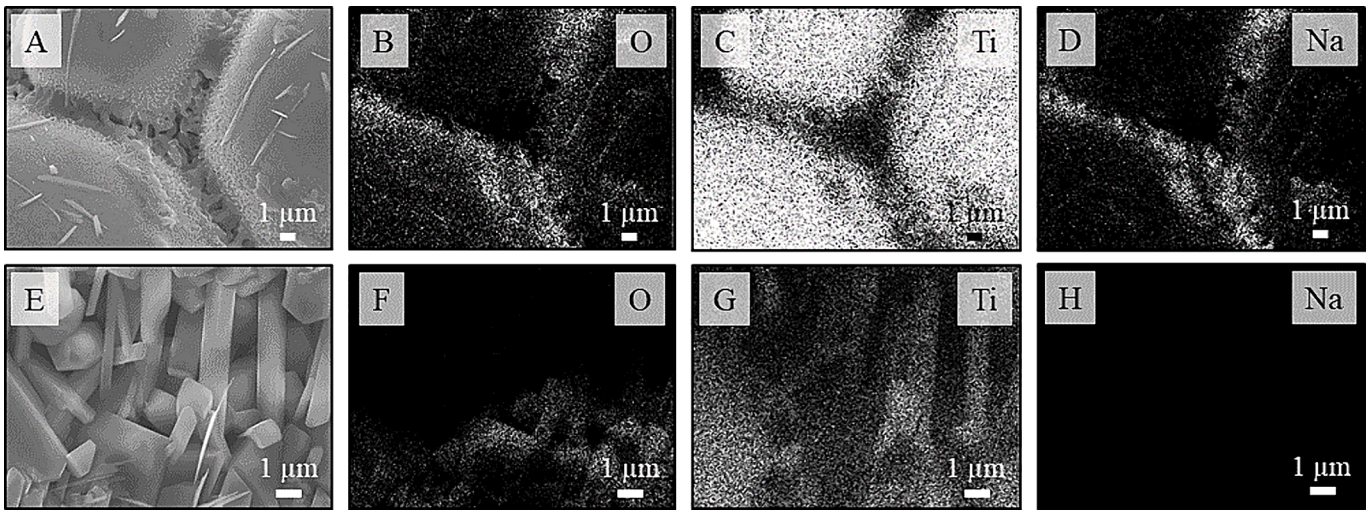

Fig. 8. SEM Micrographs (A and E) and corresponding EDS maps (B-D, D-H) of similar magnifications of porous scaffolds (Ti6Al4V_M_TC) at the point of intersection between multiple microspheres (A-D) and their heat-treated (Ti6Al4V_MS_HT) counterpart samples (E-H). Oxygen (B and F), titanium (C and G) and sodium (D and H) elements were analysed for both samples.

Table 4
EDS elemental composition of representative pre-converted Ti6Al4V powder (Ti6Al4V_MS), NaOH converted samples (Ti6Al4V_MS_TC), and heat-treated samples (Ti6Al4V_MS_HT). Values given are mean values with standard error (n = 3).

Sample	Elemental Composition (EDS)				
	Na/at.%	O/at.%	Ti/at.%	V/at.%	Al/at.%
Ti6Al4V_MS	0	0	86.2±0.2	4.1±0.1	9.7±0.1
Ti6Al4V_MS_TC	15.1±0.4	59.8±0.9	23.4±0.7	1.1±0.3	0.6±0.1
Ti6Al4V_MS_HT	Trace	31.4±4.5	65.4±4.2	2.1±0.6	1.1±0.3

peaks were noted, corresponding to the Na 1s at *ca.* 1072.3 eV and the Na KLL Auger peak at *ca.* 498 eV), with a reduction in intensity of the Ti 2p and C 1s peaks. Furthermore, after heat treatment (Ti6Al4V_MS_HT), the Na 1s and Na KLL Auger peaks both decreased in intensity, with an increase in the Ti 2p, C 1s, and O 1s peaks.

High resolution spectra of the O 1s peak (Fig. 10B) for the Ti6Al4V_MS sample contained two constituent peaks located at 530.1 (63.2 %), and 532.2 (36.8 %) eV, corresponding to O^{2-} (M^{x+}—O_x; M = Ti, Al, V), and OH− (M^{x+}—$(OH)_x$; M = Ti, Al, V). Following NaOH treatment (Ti6Al4V_MS_TC), the number of deconvoluted peaks increased to four, corresponding to O^{2-} (24.5 %; Ti^{4+}—O), OH− (46.5 %; Ti^{4+}—OH), H_2O (14.4 %), and Na KLL (14.6 %) located at 530.7, 532.6, 534.1 and 536.6 eV, respectively. After subsequent heat treatment (Ti6Al4V_MS_HT), the number of deconvoluted peaks was reduced to two, corresponding to the same states as the Ti6Al4V_MS powder above, with peaks located at 530.1 and 532.0 eV, respectively. The total oxygen content for the samples exhibited subtle changes due to the treatments conducted (Table 6). The Ti6Al4V_MS powder contained *ca.* 71.7 at.%, which increased to *ca.* 77.0 at.% following NaOH treatment (Ti6Al4V_MS_TC), and again to *ca.* 80.9 at.% following heat treatment (Ti6Al4V_MS_HT).

For the Ti 2p doublet (Fig. 10C), there was no significant alterations to the peak positions or components in any of the samples tested. All samples only contained Ti in its 4+ valence state (TiO_2) located at 458.5, 458.8, and 458.3 eV for the Ti6Al4V_MS, Ti6Al4V_MS_TC, and Ti6Al4V_MS_HT samples, respectively. The total Ti content for the samples exhibited significant changes due to the treatments conducted (Table 6). The Ti6Al4V_MS powder contained *ca.* 28.3 at.%, which decreased to just *ca.* 3.9 at.% following NaOH treatment (Ti6Al4V_MS_TC), but increased to *ca.* 13.1 at.% following heat treatment (Ti6Al4V_MS_HT).

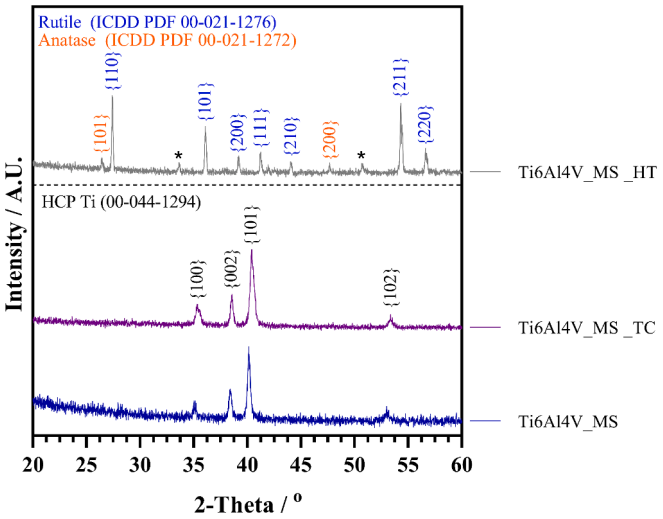

Fig. 9. XRD spectra of the Ti6Al4V powder (Ti6Al4V_MS), NaOH converted scaffold (Ti6Al4V_MS_TC), and the heat-treated scaffold (Ti6Al4V_MS_HT). unattributed peaks marked *.

Na 1s high resolution data (Fig. 10D) demonstrated noticeable variations in peak components and peak positions, (note the Na 1 s peak exhibits overlapping of the Ti LMM Auger peaks). For the Ti6Al4V_MS sample, only the Ti Auger peaks were presented, however, upon conversion an identifiable peak corresponding to Na 1s appeared, located at 1072.3 eV (Na—O; 80.8 %). Furthermore, following heat treatment, a shift in position to 1071.6 eV was seen, with a reduction in the relative proportion to 61.3 %. Converse trends were noted regarding the total Na content relative to the Ti content of the samples tested. The Ti6Al4V_MS powder contained no Na, which increased to just *ca.* 19.1 at.% following NaOH treatment (Ti6Al4V_MS_TC), but decreased to *ca.* 6.0 at.% following heat treatment (Ti6Al4V_MS_HT), highlighting the concentration of Na is in the surface since EDS only demonstrated trace quantities. The reduction in Na and increase in C content in the heat treated sample is due to rutile conversion of the titanate structure and C contamination from the furnace, respectively.

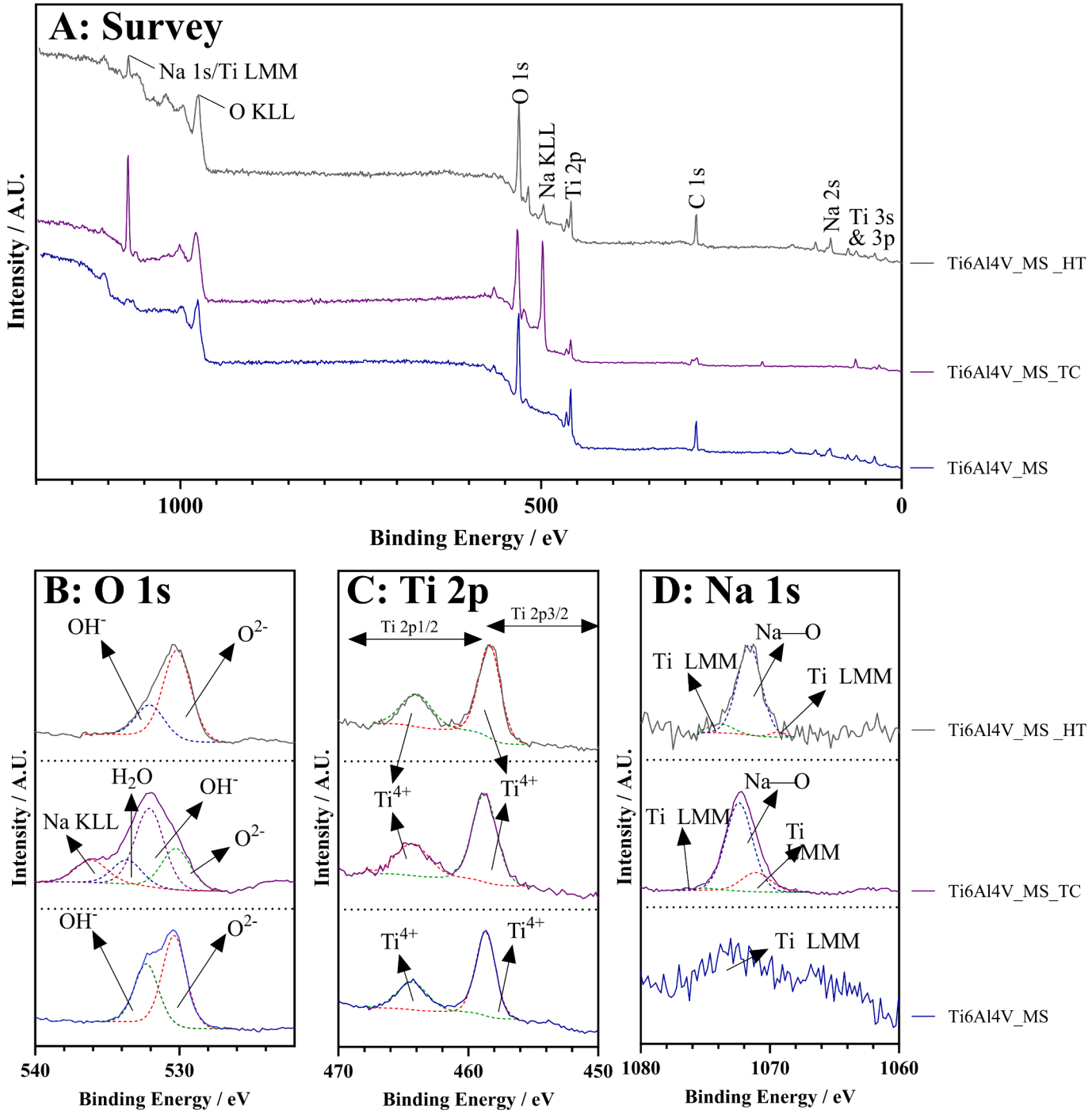

Fig. 10. XPS analysis of pre-, and post-NaOH conversion of Ti6Al4V microspheres, with additional heat treated samples. Dashed lines represent fitted components, with arrows detailing their assignment.

Table 5
Elemental states, bonding, and relative proportion data for all elements (Ti, O, Na) and samples tested.

Sample Code	Elements	Binding Energy/eV	Corresponding Bonds (Area/%)	Ref.
Ti6Al4V_MS	O 1s	530.1 (O^{2-})	M^{x+}—O (63.22)	[30,31]
		523.2 (OH^-)	M^{x+}—OH (36.78)	
	Ti 2p 3/2	458.5 (Ti^{4+})	O—Ti^{4+} (100)	[30]
Ti6Al4V_MS_TC	O 1s	530.7 (O^{2-})	Ti^{4+}—O (24.5)	[31]
		532.6 (OH^-)	Ti^{4+}—OH (46.5)	
		534.1 (H_2O)	O—H (14.4)	
		536.6 (Na KLL)	- (14.6)	
	Ti 2p 3/2	458.8 (Ti^{4+})	O—Ti^{4+} (100)	[1,2,4,32,33]
	Na 1s	1072.3	O—Na (80.8)	[1,2,4,32–34]
Ti6Al4V_MS_HT	O 1s	530.1 (O^{2-})	Ti^{4+}—O (74.4)	[31]
		532.0 (OH^-)	Ti^{4+}—OH (25.6)	
	Ti 2p 3/2	458.3 (Ti^{4+})	O—Ti^{4+} (100)	[1,2,4,32,33]
	Na 1s	1071.6	O—Na (61.3)	[1,2,4,32–34]

Table 6
XPS elemental data for the Ti6Al4V_MS, Ti6Al4V_MS_TC, Ti6Al4V_MS_HT samples. All values are the mean with associated standard deviation.

Sample	Elemental Composition (XPS)		
	Na/at.%	O/at.%	Ti/at.%
Ti6Al4V_MS	0	71.7±1.0	28.3±1.0
Ti6Al4V_MS_TC	19.1±0.4	77.0±0.5	3.9±0.2
Ti6Al4V_MS_HT	6.0±0.7	80.9±0.8	13.1±0.5

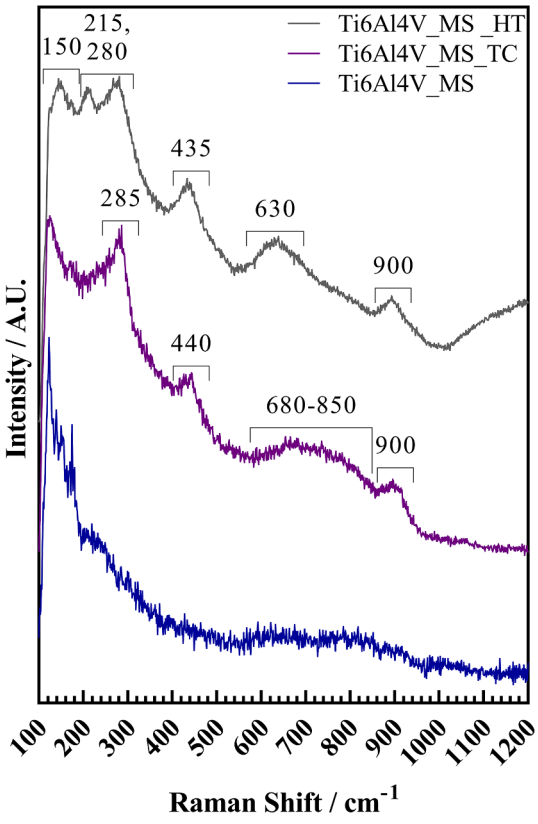

Fig. 11. Raman spectra of the Ti6Al4V_MS powder, the formed representative scaffold (Ti6Al4V_MS_TC) and the heat treated counterpart (Ti6Al4V_MS_HT).

3.7. Raman Spectroscopy

Raman spectral analysis is detailed in Fig. 11. Following NaOH treatment (Ti6Al4V_TC scaffold), peaks at *ca.* 280, 440, and 900 cm^{-1}, with broad peaks around 630–800 cm^{-1} were seen, consistent with sodium hydrogen titanate ($Na_xH_{2-x}Ti_3O_7$). Furthermore, following heat treatment (600 °C) of the scaffold (Ti6Al4V_TC_HT), further peaks in addition to the Ti6Al4V_TC sample, were located at *ca.* 150, 215, and 280 cm^{-1} corresponding to both anatase and rutile species; the 150 cm^{-1} peak related to anatase B_{1g} and E_g modes, whilst the bands at 215 and 280 cm^{-1}, correlated with anatase E_g and rutile second order phonons (Ti_2O_3), respectively.

3.8. Mechanical testing

For the compression mechanical testing (Fig. 12), all structures were assessed based on their end conditions, namely flat, porous (wide) and porous (narrow). The different testing conditions and their associated nomenclature were as follows: Ti6Al4V_MS_TC (no heat treatment); Ti6Al4V_MS_HT (600 °C heat treatment). It was found that by heat treating the flat, porous (wide) and porous (narrow) scaffolds, an increase in compressive modulus was seen, from 2.2±1.1 to 8.4±0.2, 1.6 ±0.6 to 16.5±3.2, and 0.6±0.4 to 26.6±10.2 MPa, respectively. The large error associated with the heat treated porous narrow samples was

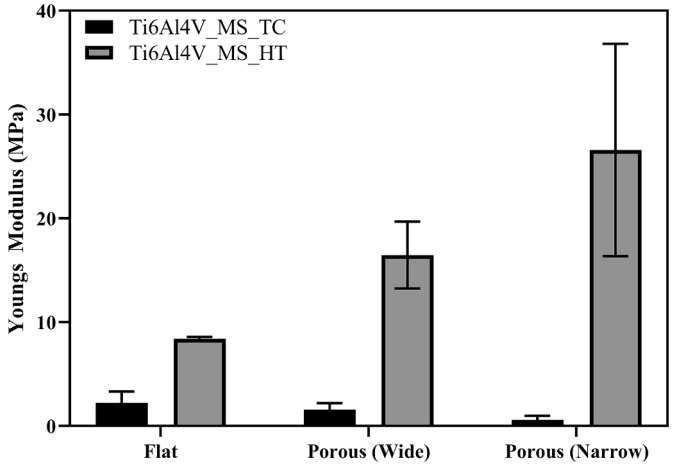

Fig. 12. Mechanical compression testing data detailing the compressive modulii of tested structures, namely flat, porous (wide) and porous (narrow). The different testing conditions were Ti6Al4V_MS_TC (no heat treatment); Ti6Al4V_MS_HT (600 °C heat treatment).

likely due to the larger variation in porosity levels and hence their ability to deform under compressive load.

4. Discussion

The formation of porous scaffolds through the novel route highlighted in this study under optimum conditions can generate with high consistency macro-porous scaffolds held together *via* bonding of alkaline titanate structures on Ti6Al4V microspheres. From the initial data regarding sphere:solution ratios (Fig. 3), as well as comparing narrow (15 mm) *vs.* wide (23 mm) vials, there is a clear influence on the end products due to the two main initial parameters. Firstly, looking at sphere:solution (S:S) ratios (Fig. 3), there are clear boundaries that result in three main structures (either titanate converted powder, macroporous scaffolds, and flat, compact discs) formed depending on the sphere:solution ratio, as well as the vial type used. The three classifications of formed structures were defined as follows: Flat scaffolds exhibit minimal to no macroscopic porosity, with a flat, compact disc formed; porous scaffolds demonstrate open porous structures, significantly taller than the flat scaffolds; converted powder is where no scaffold is formed, only titanate converted powder present, Fig. 2.

It is clear that a S:S ratio of >8 forms mainly flat scaffolds or powder, with wide vials preferentially forming flat scaffolds, whilst narrow vials produced powder. The likely mechanism for this is in the wide vial, when the reaction generates hydrogen gas [35], the depth of powder that is present is relatively small (*ca.* 5 mm) compared to the narrow vial (*ca.* >10 mm) in the same conditions. During titanate conversion, hydrogen gas is produced through the following reactions. Initially the

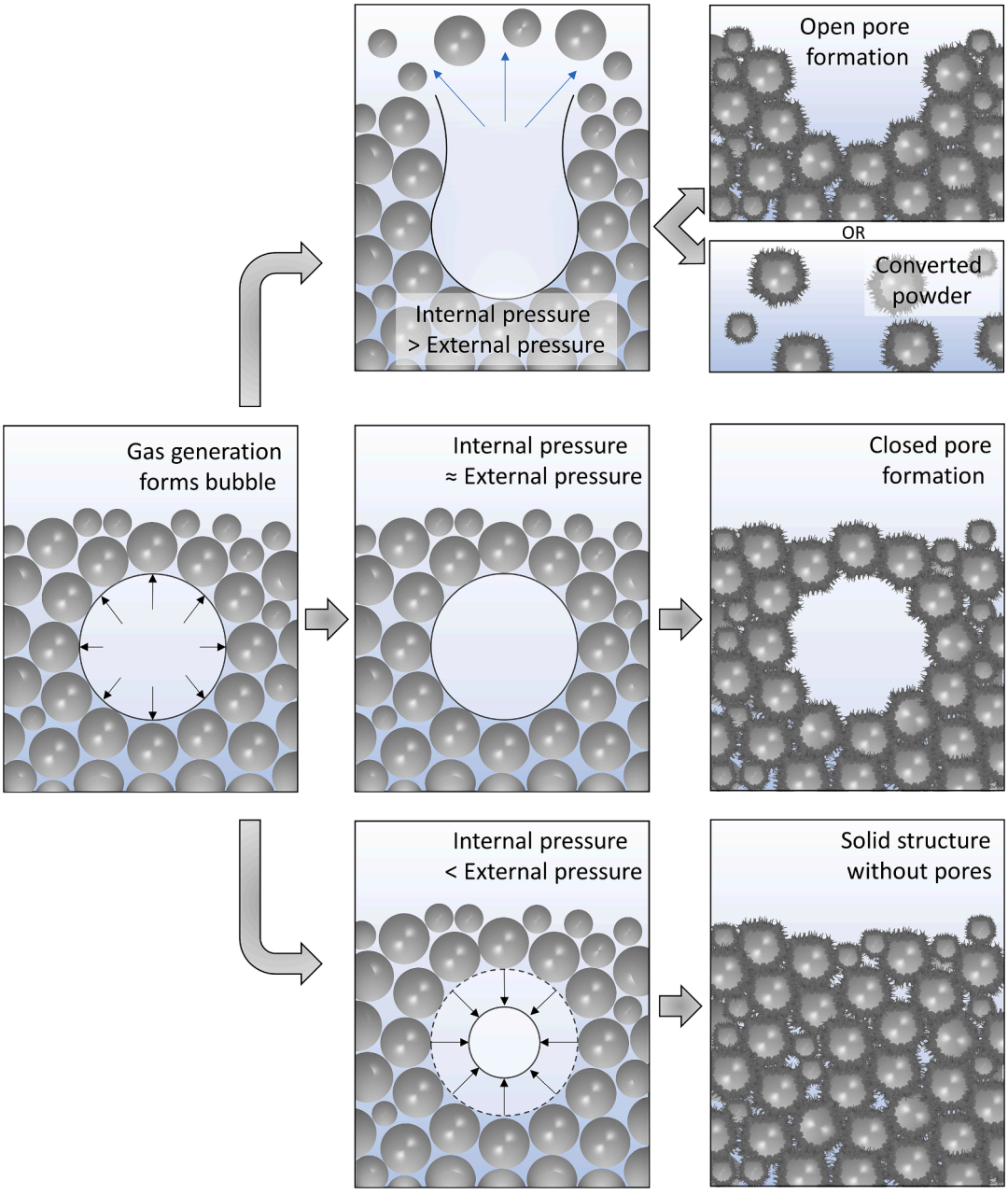

Fig. 13. Bubble formation mechanism detailing the effect of internal *vs.* external pressure of pores due to hydrogen evolution of the titanate mechanism. If the internal pressure is greater than the external, then either open pores will form, or the pressure is so significant that only converted powder will form. If the internal and external pressure are approximately equal, then closed pores are likely to form. Finally, if the internal pressure is significantly less than the external pressure, this will result in a solid structure without macroscopic pores (the surface of the spheres will be porous in the micron range due to the titanate structure).

passivated surface layer, TiO_2, is partially dissolved by the alkaline solution, Eq. (1):

$$TiO_2 + OH^- \rightarrow HTiO_3^- \quad (1)$$

The above reaction occurs concurrently with the hydration of the Ti metal [36–41]; from Eqs. (2) to (4), oxygen penetrates into the top 1 μm of the surface, with simultaneous hydrogen evolution Eq. (3).

$$Ti + 3OH^- \rightarrow Ti(OH)_3^+ + 4e^- \quad (2)$$

$$Ti(OH)_3^+ + e^- \rightarrow TiO_2.H_2O + \left(\frac{1}{2}H_2\right)\uparrow \quad (3)$$

$$Ti(OH)_3^+ + OH^- \rightarrow Ti(OH)_4 \quad (4)$$

The gas formed can readily escape in the wide vial since the pathway to the surface is small and the external pressure from the suspension is reduced due to the suspension being more spread out over the vial volume (note: narrow = Falcon™ 15 mL, 17 mm diam., 120 mm length; and wide = Nunc™ 50 mL, 30 mm diam., 90 mm length), thus preventing pore formation. Since gas can easily escape, limited macropores can be sustained during the titanate cross linking reaction, compact flat structures are more likely formed. In the narrow vial, the depth of powder is greater and hence any gas formation deeper within the structure has a longer pathway to escape. The results show an open pore formation at the vial sides indicative of the preferential pathway being horizontal rather than vertical, limiting cross-linking between microspheres, since the pores/voids formed comprise the majority of the vial diameter. Any cross-linking that did form, would be insufficient to produce stable scaffold structures.

Similarly, a ratio of $<^1/_3$ resulted in purely powder formation, which is most likely due to excessive solution resulting in too much particle mobility during hydrogen evolution. This prevented cross-linking between the particles but still allowed titanate formation on the particle surface. This was irrespective of vial size since the solution amount was significantly more than the microsphere content. There appears to be an optimal solution quantity/sphere:solution ration (*ca.* $^1/_3$) in which particle break-up rather than coalescence and self-linking is observed.

Two more transition regions were noted, where differing vial sizes/ratios generated different scaffold conditions. One porous/powder transition occured between 0.5 and $^1/_3$ ratio, whilst a porous/flat transition occurred between 3 and 8. For the porous/powder transition, porous structures tended to form in this region in the narrow vial, whilst the wide vial generated some porous structures with powder formation. In the narrow vial, the increase in powder compared to the solution quantity should have a two-fold difference: the increase in powder, results in a higher density (density of NaOH (at 20 °C) is 1.185 gcm^{-3}, whilst the density of Ti6Al4V is 4.41 gcm^{-3}), preventing gas release whilst stabilising pore formation, especially since the narrow vial results in larger depth of powder for the gas to escape. Secondly, the distribution of solution through the powder is more optimal enabling sufficient reaction and cross-linking without the need for additional agitation. In the wide (50 mL) vial, this partially occurs, however, the depth of powder is smaller, meaning that formed gas can escape more easily, contributing to both pore formation, but also powder formation. The second transition region between the S:S ratios of 3 and 8 resulted in various structures of either porous or flat scaffold formation. Only wide vials were used in this region since the narrow vial prevented ingress of the solution to all the powder for the entire reaction time (24 h); gravity resulted in pooling of the solution in the base of the vial.

A possible pore forming mechanism is illustrated in Fig. 13. Bubbles in viscous fluids generally attain a spherical shape as their hydrodynamics are largely dominated by the surface tension and the viscous forces of the liquid phase. The gas forming from the titanate formation reaction coalesces to reduce the surface energy, with subsequent gas formation diffusing to already present pore nuclei [42]. If these forces are in balance for long enough to provide a stable foam prior to cross-linking, then a porous structure will form. As described by Stevenson [43], Ostwald ripening [44], also known as inter-bubble gas diffusion, of gas–liquid foam is the process by which big bubbles consume adjacent smaller bubbles. This occurs due to differences in pressure in the two bubbles caused by the Young–Laplace effect [45]. Since, the pressure within the smaller bubble is higher than the larger one, this drives transport of the gas out of the small bubble and into the bigger one. This mechanism links well with the perceived structure differences attained via the variations in sphere:solution ratios, which in turn have different solution viscosities. For porous structures to form, the pressure of gas bubbles formed must be relatively equivalent to the pressure of the surrounding powder/solution otherwise the gas would escape readily forming very open pores or powder. If the external pressure is greater than the internal pressure of the gas bubbles, a flat dense structure with limited porosity and smaller pores or powder would be obtained (Fig. 13). There is clearly an optimal region where porous scaffold formation is mostly seen in both vial types, and hence this region has optimal sphere:solution ratio and vial conditions to enable pore formation, and proximity of spheres to generate sufficient crosslinking to produce stable scaffold formation.

Similar to conventional gas foaming techniques [46], whereby N_2 or CO_2 gas is utilised to generate pores in polymeric structures, this methodology is reliant on gas bubble movement and stability in order to produce porous structures. However, in conventional gas foaming techniques, as described by Dehghani et al. [46], inhomogeneous foam formation with a non-porous bottom layer and highly porous top surface is seen, due to significant differences in gas and liquid densities. Despite the differences in density for the method described here, due to simultaneous gas formation of all reacting microsphere surfaces, this enables relatively consistent pore formation throughout the structures generated, as illustrated in the MicroCT data (Fig. 7). Morphologically, the flat structures are composed of interconnected microspheres, between the titanate struts, which extends the initial findings from the present authors in a previous study [25]. The cross-linked area between the microspheres appears denser than the converted microspheres alone due to interlinking and physical bonding between the titanate surfaces. It is likely this occurs since the proximity prevents the potential growth of the titanate structures and hence rather than the reaction progressing to extend the struts, energy is shifted towards perpendicular growth. In the porous scaffolds, formed pores are spherical in nature, which indicates the pore formation is due to gas bubble growth since bubbles grow to minimise surface area due to surface tension [47], with diameters of *ca.* 100–200 μm. Microspheres exhibit extensive cross linking, with significant struts between microspheres (*ca.* 200 nm diam.). Pores are surrounded by connected microspheres, so bubble formation needs to be sufficiently held to enable cross-linking to occur. Once initial cross linking has occurred, gas escape is possible due to the porosity, and additional solution presence may enable further reaction to form thicker interconnected struts.

Chemically, the titanate converted powders and scaffolds formed the characteristic titanate formation as seen in previous studies and have been compiled in [5]. XPS (Table 6) and EDS (Table 4) demonstrated increases in Na content, with concentration of Na at the surface (*ca.* 19.1 at% in XPS *vs.* 15.1 at% in EDS). The surface layer was too thin to be seen via XRD (Fig. 9), hence only Ti peaks being present. Heat treatment resulted in rutile formation, with thick (1 μm) crystals. These replaced the majority of internal pores, however, on the order of 50 external pores remained (Fig. 5). There was a notable loss of the Na KLL peak in the heat-treated sample (Fig. 10), however Na—O is still present, which may be due to the reduction in Na content in the surface from rutile formation. Raman (Fig. 11), XPS and EDS all agree, with XRD only showing Ti with rutile formation following heat treatment. The heat treatment had a significant effect on the compressive mechanical properties of the scaffolds, which is likely due to the rutile formation spanning the cross-linked microspheres.

Mechanically, it is evident that by heat treating the sample, one can see a marked increase in the compressive mechanical properties for all sample types. The improvement was minimal for the flat scaffolds since the lack of porosity prevented further available compression of the scaffold before crushing of microspheres occurred. The flat scaffolds prior to heat treatment performed better than the porous counterparts, since the titanate cross-linked surfaces are relatively weak between pores compared to a compact structure of microspheres seen in the flat samples. The heat treatment was employed as a method of improving the mechanical properties of the scaffolds, since the cross-linked titanate structures are converted into rutile crystals. It is evident that this worked to some degree, placing these in similar compressive values to that of other biomedical scaffolds in the literature, however, this is only for compressive loads.

Finally, regarding porosity differences between the formed structures and the effect the heat treatment had on the porosity, a number of interesting observations were noted. Comparison between the termed 'Porous' (demonstrating pores on the macro scale) and 'Flat' (denser, with limited to no microporosity), scaffolds demonstrated a clear drop in the average pore size, from 6.01 ($\pm$2.50) $\times$ 10^8 to 0.72 ($\pm$0.03) $\times$ 10^8 and is a direct result of the mechanism outlined above. It is expected that the level of porosity drops from the porous to flat samples, since there is a significant drop in scaffold height between the two samples, and the external surface displays minimal porosity for the flat samples compared to the open porous counterparts. Heat treatment of the scaffolds also demonstrates a significant effect on the level of porosity noted. For both the porous and flat scaffolds, their heat treated counterparts show a decrease in average pore volumes (6.01 ($\pm$2.50) $\times$ 10^8 *vs.* 2.17 ($\pm$0.46) $\times$ 10^8 for the Porous and Porous Heat Treated scaffolds, respectively, and 0.72 ($\pm$0.03) $\times$ 10^8 *vs.* 0.23 ($\pm$0.05) $\times$ 10^8 for the Flat and Flat Heat Treated scaffolds, respectively). Again, this makes sense since during the heat treatment stage, as confirmed via EDS, XRD, and XPS (Fig. 8, Fig. 9, and Fig. 10, respectively), rutile (TiO_2) crystals have grown in place of the original titanate structures. This growth is more likely to expand into the pores formed since they are unimpeded, thus reducing the pore volume. It is also evident from the SEM image (Fig. 5) of the heat treated sample compared to the non-heat treated scaffold (Fig. 4) at the same scale, the areas where pores were are solely made up of rutile crystals.

Ultimately, this study demonstrates the optimal conditions necessary for generating optimised hierarchically porous scaffolds. The potential for these structures is wide ranging from water treatment, such as filters for heavy metal treatment, to biomedical, such as bone plugs for voids produced via osteoporosis. By having a hierarchically porous structure, it benefits orthopaedic applications [48], since the larger, macropores provide ingrowth of osteoblasts, whilst the smaller micro/nanopores, facilitate better mechanical interlocking once new bone has formed. The alkali titanate surface also facilitates the absorbance of ions from water [49], as well as enabling bone growth through ion-exchange reactions [5]. The ability to generate hierarchically porous scaffolds, which have wide-ranging potential, in a simple and cost-effective manner is advantageous over other techniques, such as additive manufacturing, however, further optimisation of the mechanical properties and biological effects must be considered if to be used in a biomedical context.

5. Conclusions

This study highlights the promising formation of 3D hierarchically porous scaffolds through cross-growth and merging of sodium titanate surfaces on Ti alloy microspheres. The chemical, structural, morphological properties, as well as the formation mechanism identified in this study, demonstrates the key formation conditions required to consistently generate such structures, and the likely levels of porosity and mechanical properties of these generated structures. It was clear, as evidenced from the data, successful formation of a titanate layer was produced on the Ti6Al4V microspheres, as confirmed in previous studies. The formation of sodium titanate on the surface of the microspheres, as confirmed by XPS, EDS and Raman, resulted in cross-linking between the microspheres. Gas formation from the sodium titanate conversion mechanism was found to be the most important factor in pore formation, which was heavily influenced by the type of vial (wide *vs.* narrow) used, and the sphere:solution ratio.

The formed structures were categorised into three common subtypes, with their ideal sphere:solution (g:mL) ratios being: 1) unbonded, sodium titanate-converted microspheres ($<^1/_3$ and >8); 2) flat (non-macroporous) scaffolds (>3 and <8); or 3) open, hierarchically porous scaffolds (between 0.5 and 3). Certain structures formed due to a combination of microsphere freedom of movement, H_2 gas bubble formation, and exposed surface reactivity. This promising discovery highlights the potential for lower temperature, simplistic production of 3D constructs with modifiable chemical properties due to the ion-exchange potential of titanate structures, with clear applications in a wide-range of fields. The applicability of the nanoporous sodium titanate scaffolds formed should certainly be investigated for biomedical, electrocatalysis, and water treatment applications, as well as comparing this to the state-of-the-art for that particular field.

CRediT authorship contribution statement

Matthew D. Wadge: Writing – review & editing, Writing – original draft, Validation, Supervision, Project administration, Methodology, Investigation, Funding acquisition, Formal analysis, Data curation, Conceptualization. **Pearl A. Agyakwa:** Writing – review & editing, Investigation, Formal analysis, Data curation. **Reda M. Felfel:** Writing – review & editing, Supervision, Methodology, Investigation, Formal analysis, Data curation, Conceptualization. **Richard Homer:** Writing – review & editing, Resources, Formal analysis, Data curation. **Timothy P. Cooper:** Writing – review & editing, Writing – original draft, Methodology, Investigation, Formal analysis, Data curation. **Zakhar R. Kudrynskyi:** Writing – review & editing, Writing – original draft, Methodology, Investigation, Formal analysis, Data curation. **Edward Lester:** Writing – review & editing, Supervision. **Ifty Ahmed:** Writing – review & editing, Supervision. **David M. Grant:** Writing – review & editing, Writing – original draft, Supervision, Project administration, Methodology, Investigation, Conceptualization.

Declaration of competing interest

The authors declare that they have no known competing financial interests or personal relationships that could have appeared to influence the work reported in this paper.

Data availability

Data will be made available on request.

Acknowledgements

This work was graciously funded through an Engineering and Physical Sciences Research Council (EPSRC) Doctoral Prize Fellowship [grant number EP/T517902/1], as well as support from an EPSRC equipment grant [grant number EP/L022494/1]. Dr Z.R. Kudrynskyi acknowledges funding through a Nottingham Research Fellowship from the University of Nottingham. The authors would like to thank all technical help within the Wolfson building and nmRC facilities at the University of Nottingham, as well as Dr Martin Corfield for their help in capturing the MicroCT data and Dr Nesma Aboulkhair for providing the Ti64 powder.

Appendix A. Supplementary data

Supplementary data to this article can be found online at https://doi.org/10.1016/j.matdes.2024.112835.

References

[1] H.M. Kim, F. Miyaji, T. Kokubo, T. Nakamura, Preparation of bioactive ti and its alloys via simple chemical surface treatment, J Biomed Mater Res 32 (3) (1996) 409–417.

[2] T. Kokubo, F. Miyaji, H.-M. Kim, T. Nakamura, Spontaneous formation of bonelike apatite layer on chemically treated titanium metals, Journal of the American Ceramic Society 79 (4) (1996) 1127–1129.

[3] H.-M. Kim, F. Miyaji, T. Kokubo, T. Nakamura, Apatite-forming ability of alkali-treated ti metal in body environment, Journal of the Ceramic Society of Japan 105 (1218) (1997) 111–116.

[4] H. Kim, F. Miyaji, T. Kokubo, T. Nakamura, Effect of heat treatment on apatite-forming ability of ti metal induced by alkali treatment, Journal of Materials Science: Materials in Medicine 8 (6) (1997) 341–347.

[5] M.D. Wadge, J. McGuire, K.G. Thomas, B.W. Stuart, R.M. Felfel, I. Ahmed, D. M. Grant, Developing alkaline titanate surfaces for medical applications, International Materials Reviews (2023) 1–48.

[6] Y. Tang, L. Chen, Z. Duan, K. Zhao, Z. Wu, Graphene/barium titanate/polymethyl methacrylate bio-piezoelectric composites for biomedical application, Ceramics International 46 (5) (2020) 6567–6574.

[7] S. Sahoo, A. Sinha, M. Das, Synthesis, characterization and in vitro biocompatibility study of strontium titanate ceramic: a potential biomaterial, J Mech Behav Biomed Mater 102 (2020) 103494.

[8] M. Zhang, Z. Gong, J. Zhang, H. Cheng, J. Chen, Y. Zeng, Z. Zhu, Y. Wan, Engineered zinc titanate coatings on the titanium Surface with enhanced antitumor properties and biocompatibility, ACS Biomater Sci Eng 5 (11) (2019) 5935–5946.

[9] S. Yamaguchi, P. Thi Minh Le, M. Ito, S.A. Shintani, H. Takadama, Tri-functional calcium-deficient calcium titanate coating on titanium metal by chemical and heat treatment, Coatings 9 (9) (2019) 561.

[10] M. Gathen, M.M. Ploeger, M. Jaenisch, S. Koob, D. Cucchi, A. Kasapovic, T. Randau, R. Placzek, Outcome evaluation of new calcium titanate schanz-screws for external fixators. first clinical results and cadaver studies, Journal of Materials Science: Materials in Medicine 30 (11) (2019) 1–8.

[11] S. Phromyoo, N. Lertcumfu, P. Jaita, P. Jarupoom, K. Pengpat, G. Rujijanagul, Effects of barium zirconium titanate on the properties of β-tricalcium phosphate bioceramics, Ceramics International 44 (3) (2018) 2661–2667.

[12] M.D. Wadge, B. Turgut, J.W. Murray, B.W. Stuart, R.M. Felfel, I. Ahmed, D. M. Grant, Developing highly nanoporous titanate structures via wet chemical conversion of DC magnetron sputtered titanium thin films, Journal of Colloid and Interface Science 566 (2020) 271–283.

[13] M.D. Wadge, B.W. Stuart, K.G. Thomas, D.M. Grant, Generation and characterisation of gallium titanate surfaces through hydrothermal ion-exchange processes, Materials & Design 155 (2018) 264–277.

[14] M.D. Wadge, J. McGuire, B.V.T. Hanby, R.M. Felfel, I. Ahmed, D.M. Grant, Tailoring the degradation rate of magnesium through biomedical nano-porous titanate coatings, Journal of Magnesium and Alloys 9 (1) (2021) 336–350.

[15] S. Yamaguchi, S. Nath, Y. Sugawara, K. Divakarla, T. Das, J. Manos, W. Chrzanowski, T. Matsushita, T. Kokubo, Two-in-one Biointerfaces-antimicrobial and bioactive nanoporous gallium titanate layers for titanium implants, Nanomaterials (basel) 7 (8) (2017) 229.

[16] S. Yamaguchi, S. Nath, T. Matsushita, T. Kokubo, Controlled release of strontium ions from a bioactive ti metal with a ca-enriched surface layer, Acta Biomater 10 (5) (2014) 2282–2289.

[17] A. Cochis, B. Azzimonti, C. Della Valle, E. De Giglio, N. Bloise, L. Visai, S. Cometa, L. Rimondini, R. Chiesa, The effect of silver or gallium doped titanium against the multidrug resistant Acinetobacter baumannii, Biomaterials 80 (2016) 80–95.

[18] K. Hamada, M. Kon, T. Hanawa, K.i. Yokoyama, Y. Miyamoto, K. Asaoka, Hydrothermal modification of titanium surface in calcium solutions, Biomaterials 23 (10) (2002) 2265–2272.

[19] H. Eslami, F. Moztarzadeh, T.S.J. Kashi, K. Khoshroo, M. Tahriri, Hydrothermal synthesis and Characterization of TiO2-derived nanotubes for biomedical applications, Synthesis and Reactivity in Inorganic, Metal-Organic, and Nano-Metal Chemistry 46 (8) (2016) 1149–1156.

[20] G.-S. Kim, H.-K. Seo, V.P. Godble, Y.-S. Kim, O.B. Yang, H.-S. Shin, Electrophoretic deposition of titanate nanotubes from commercial titania nanoparticles: application to dye-sensitized solar cells, Electrochemistry Communications 8 (6) (2006) 961–966.

[21] L. Torrente-Murciano, A.A. Lapkin, D. Chadwick, Synthesis of high aspect ratio titanate nanotubes, Journal of Materials Chemistry 20 (31) (2010) 6484–6489.

[22] A.L. Papa, L. Dumont, D. Vandroux, N. Millot, Titanate nanotubes: towards a novel and safer nanovector for cardiomyocytes, Nanotoxicology 7 (6) (2013) 1131–1142.

[23] A.L. Papa, J. Boudon, V. Bellat, A. Loiseau, H. Bisht, F. Sallem, R. Chassagnon, V. Berard, N. Millot, Dispersion of titanate nanotubes for nanomedicine: comparison of PEI and PEG nanohybrids, Dalton Trans 44 (2) (2015) 739–746.

[24] H. Zhao, W. Dong, Y. Zheng, A. Liu, J. Yao, C. Li, W. Tang, B. Chen, G. Wang, Z. Shi, The structural and biological properties of hydroxyapatite-modified titanate nanowire scaffolds, Biomaterials 32 (25) (2011) 5837–5846.

[25] M.D. Wadge, M.J. Carrington, H. Constantin, K. Orange, J. Greaves, M.T. Islam, K. M.Z. Hossain, T.P. Cooper, Z.R. Kudrynskyi, R.M. Felfel, I. Ahmed, D.M. Grant, Characterization of potential nanoporous sodium titanate film formation on Ti6Al4V and TiO2 microspherical substrates via wet-chemical alkaline conversion, Materials Characterization 185 (2022) 111760.

[26] M.D. Wadge, M.A. Bird, A. Sankowski, H. Constantin, M.W. Fay, T.P. Cooper, J. N. O'Shea, A.N. Khlobystov, D.A. Walsh, L.R. Johnson, Nanostructured, alkaline titanate-converted, and heat-treated Ti6Al4V microspheres via wet-chemical alkaline modification and their ORR electrocatalytic response, Advanced Materials Interfaces 10 (5) (2023) 2201523.

[27] C. Phutela, N.T. Aboulkhair, C.J. Tuck, I. Ashcroft, The effects of feature sizes in selectively laser melted ti-6Al-4V parts on the validity of optimised process parameters, Materials 13 (1) (2020) 117.

[28] C. Giannini, M. Ladisa, D. Altamura, D. Siliqi, T. Sibillano, L. De Caro, X-ray diffraction: a powerful technique for the multiple-length-scale structural analysis of nanomaterials, Crystals 6 (8) (2016) 87.

[29] M.A. Surmeneva, R.A. Surmenev, E.A. Chudinova, A. Koptioug, M.S. Tkachev, S. N. Gorodzha, L.-E. Rännar, Fabrication of multiple-layered gradient cellular metal scaffold via electron beam melting for segmental bone reconstruction, Materials & Design 133 (2017) 195–204.

[30] U. Diebold, T. Madey, TiO2 by XPS, Surface Science Spectra 4 (3) (1996) 227–231.

[31] P. Krishnan, M. Liu, P.A. Itty, Z. Liu, V. Rheinheimer, M.-H. Zhang, P.J. Monteiro, E.Y. Liya, Characterization of photocatalytic TiO_2 powder under varied environments using near ambient pressure X-ray photoelectron spectroscopy, Scientific Reports 7 (2017) 43298.

[32] J.F. Moulder, W.F. Stickle, P.E. Sobol, K.D. Bomben, Handbook of X-ray photoelectron spectroscopy: a reference book of standard spectra for identification and interpretation of XPS data, Perkin-Elmer Co., Minnesota, U.S.A, 1995.

[33] H.M. Kim, F. Miyaji, T. Kokubo, S. Nishiguchi, T. Nakamura, Graded surface structure of bioactive titanium prepared by chemical treatment, journal of biomedical materials Research: an official journal of the Society for Biomaterials, the japanese Society for Biomaterials, and the australian society for, Biomaterials 45 (2) (1999) 100–107.

[34] R.A. Zarate, S. Fuentes, A.L. Cabrera, V.M. Fuenzalida, Structural characterization of single crystals of sodium titanate nanowires prepared by hydrothermal process, Journal of Crystal Growth 310 (15) (2008) 3630–3637.

[35] V. Huynh, N.K. Ngo, T.D. Golden, Surface activation and pretreatments for biocompatible metals and alloys used in biomedical applications, International Journal of Biomaterials 2019 (2019).

[36] T. Hurlen, W. Wilhelmsen, Passive behaviour of titanium, Electrochimica Acta 31 (9) (1986) 1139–1146.

[37] L.D. Arsov, C. Kormann, W. Plieth, In situ raman spectra of anodically formed titanium dioxide layers in solutions of H 2 SO 4, KOH, and HNO 3, Journal of the Electrochemical Society 138 (10) (1991) 2964–2970.

[38] F. Miyaji, X. Zhang, T. Yao, T. Kokubo, C. Ohtsuki, T. Kitsugi, T. Yamamuro, T. Nakamura, Chemical treatment of Ti metal to induce its bioactivity, Bioceramics: Proceedings of the 7th International Symposium on Ceramics in Medicine, Elsevier, 1994, pp. 119-124.

[39] P. Tengvall, I. Lundström, Physico-chemical considerations of titanium as a biomaterial, Clinical Materials 9 (2) (1992) 115–134.

[40] K.E. Healy, P. Ducheyne, The mechanisms of passive dissolution of titanium in a model physiological environment, J Biomed Mater Res 26 (3) (1992) 319–338.

[41] K. Healy, P. Ducheyne, Passive dissolution kinetics of titanium in vitro, Journal of Materials Science: Materials in Medicine 4 (2) (1993) 117–126.

[42] A.I. Ansari, N.A. Sheikh, A review of bone regeneration mechanisms and bone scaffold fabrication techniques (conventional and non-conventional), Journal of the Institution of Engineers (india): Series C 103 (6) (2022) 1485–1513.

[43] P. Stevenson, Inter-bubble gas diffusion in liquid foam, Current Opinion in Colloid & Interface Science 15 (5) (2010) 374–381.

[44] J. Marqusee, J. Ross, Theory of ostwald ripening: competitive growth and its dependence on volume fraction, The Journal of Chemical Physics 80 (1) (1984) 536–543.

[45] S. Vafaei, D. Wen, Modification of the young-Laplace equation and prediction of bubble interface in the presence of nanoparticles, Advances in Colloid and Interface Science 225 (2015) 1–15.

[46] F. Dehghani, N. Annabi, Engineering porous scaffolds using gas-based techniques, Current Opinion in Biotechnology 22 (5) (2011) 661–666.

[47] R. Davies, G.I. Taylor, The mechanics of large bubbles rising through extended liquids and through liquids in tubes, Proceedings of the Royal Society of London. Series A. Mathematical and Physical Sciences 200(1062) (1950) 375-390.

[48] Z. Jia, M. Li, P. Xiu, X. Xu, Y. Cheng, Y. Zheng, T. Xi, S. Wei, Z. Liu, A novel cytocompatible, hierarchical porous Ti6Al4V scaffold with immobilized silver nanoparticles, Materials Letters 157 (2015) 143–146.

[49] N. Li, L. Zhang, Y. Chen, Y. Tian, H. Wang, Adsorption behavior of cu (II) onto titanate nanofibers prepared by alkali treatment, Journal of Hazardous Materials 189 (1–2) (2011) 265–272.